# Astrophysical $S$-Factor measurement of the $^{14}$N$(p,\gamma)^{15}$O reaction in the CNO cycle

B. Frentz,[1,2] A. Aprahamian,[1,2] A. Boeltzig,[1,2] R.J. deBoer,[1,2] J. Görres,[1,2] D. Robertson,[1,2]
M. Wiescher,[1,2] T. Borgwardt,[3,4] M. Hanhardt,[3,4] T. Kadlecek,[3,4] and F. Strieder[3,4]

[1]*Department of Physics, University of Notre Dame, Notre Dame, Indiana 46556 USA*
[2]*The Joint Institute for Nuclear Astrophysics, University of Notre Dame, Notre Dame, Indiana 46556, USA*
[3]*Department of Physics, South Dakota School of Mines & Technology, Rapid City, SD 57701, USA*
[4]*Sanford Underground Research Facility, Lead, SD 57754, USA*
(Dated: April 27, 2021)

The CNO cycle is the main energy source in massive stars during their hydrogen burning phase, but it also contributes to the energy production in our sun at the $\approx 1\%$ level. The $^{14}$N$(p,\gamma)^{15}$O reaction is the slowest reaction in the cycle and such determines the energy production rate but also the rate by which CNO neutrinos contribute to the solar neutrino flux. The CNO neutrinos come primarily from the $\beta$ decay of $^{15}$O and to a lesser extent from the decay of $^{13}$N. The direct measurement of the CNO neutrinos would provide independent new information on the metalicity of the solar core. Recently the first CNO neutrinos from $^{15}$O have been identified with the Borexino neutrino detector at the INFN Gran Sasso underground laboratory. There are still considerable uncertainties in the rate for the $^{14}$N$(p,\gamma)^{15}$O reaction at solar temperature conditions. The here presented low energy reaction data, taken at the US CASPAR underground accelerator aim at a solution of existing discrepancies in the data sets towards a better understanding of the low energy cross section of the $^{14}$N$(p,\gamma)^{15}$O reaction. The CASPAR measurements across proton energies between 0.270 and 1.070 MeV close a critical gap in the overall data and reduces the presently existing uncertainties in the reaction rate predictions.

PACS numbers: Valid PACS appear here

## I. INTRODUCTION

Solar neutrinos are primarily produced by the pp-chains which dominate nucleosynthesis - the conversion of hydrogen to helium - and energy production in our sun.[1?, 2]. The second mechanism to concert hydrogen to helium are the CNO cycles, a catalytic sequence of proton capture reactions and $\beta$ decays on C, N. and O isotopes; dominated by the primary CNO-I sequence $^{12}$C(p,$\gamma$)$^{13}$N($\beta^+\nu$)$^{13}$C(p,$\gamma$)$^{14}$N(p,$\gamma$)$^{15}$O($\beta^+\nu$)$^{15}$N(p,$\alpha$)$^{12}$C. The main source for the CNO neutrino production is the $\beta$-decay of the $^{13}$N and $^{15}$N isotopes.

Of these, the $^{14}$N$(p,\gamma)^{15}$O reaction is the slowest, rate-limiting step in the whole process, causing a gradual enrichment of $^{14}$N in the solar material. This and the shorter lifetime of $^{15}$O versus $^{13}$N suggests that CNO neutrinos will be dominated by the $\beta$ decay of $^{15}$O. In the standard solar model [3, 4], one of the major uncertainties in the description of the sun's interior is the metallicity of the solar core, which is determined by its carbon, nitrogen, and oxygen content [5]. The expected elemental abundances, based on the spectroscopic analysis of the solar atmosphere, disagree with the solar profiles of sound speed and density as well as the depth of the convective zone and the helium abundance obtained by helioseismology measurements [6]. It has been pointed out that a direct study of the CN neutrinos, coming from the $\beta$ decay of $^{13}$N and $^{15}$O, can provide an independent measure of the solar metallicity [7]. However, the CN neutrino flux not only depends on the CN abundance in the solar interior, but also on the associated CN reaction rates, such as $^{12}$C$(p,\gamma)^{13}$N and $^{14}$N$(p,\gamma)^{15}$O respectively,

as the CN neutrino flux comes arises from the $\beta$ decay of $^{13}$C and $^{15}$O.

The first comprehensive study of the $^{14}$N$(p,\gamma)^{15}$O reaction was performed by Schröder et al. [8], which reported both excitation functions and angular distributions, covering the proton energy range from $E_p = 0.2$ to 3.6 MeV. The total $S$-factor at zero energy, $S(0)$, was determined to be $3.20 \pm 0.54$ keV b, where the transitions to the ground state and to the $E_x = 6.79$ MeV excited state in $^{15}$O were dominant, contributing $S_{g.s.}(0) = 1.55 \pm 0.34$ keV b and $S_{6.79}(0) = 1.41 \pm 0.02$ keV b, respectively. Fig. 1 depicts the level structure of the $^{15}$O compound nucleus near the proton separation energy and shows these two important states.

An $R$-matrix analysis by Angulo and Descouvemont [9] drastically changed the extrapolated $S$-factor for both transitions to $S_{g.s.}(0) = 0.08^{+0.13}_{-0.06}$ keV b and $S_{6.79}(0) = 1.63 \pm 0.17$ keV b. Overall, this reduced the total $S$-factor by a factor of 1.7. A number of more recent measurements at the LUNA underground accelerator [10–13] expanded the reaction data to lower energies, suggesting an even lower $S$-factor, while an independent study Runkle et al. [14] indicated a higher value for the ground state transition. Altogether, the reported $S$ factors extrapolated to zero energy from different measurements are summarized in Table I.

An independent $R$-matrix analysis of the various reaction channels over a wide range of energies by Azuma et al. [18] incorporated more data sets and found results in best agreement with Imbriani et al. [10], although with a slightly higher zero-energy $S$ factor for the ground state transition at $S_{g.s.}(0) = 0.28$ keV b.

TABLE I: A summary of previous $S$-factor determinations. a) $R$-matrix analysis on available data, not a measurement. b) Adopted from Angulo *et al.* [9]. c) Measured $S$-factor at 70 keV. d) Calculated difference of the total $S(0)$ from the other transitions.

| Year | Reference | Astrophysical $S$-factor $S(0)$ (keV b) | | | | |
| | | R/DC $\rightarrow$ 0.00 | R/DC $\rightarrow$ 6.79 | R/DC $\rightarrow$ 6.17 | Others[d] | Total |
|---|---|---|---|---|---|---|
| 1987 | Schröder *et al.* [8] | $1.55 \pm 0.34$ | $1.41 \pm 0.02$ | $0.14 \pm 0.05$ | 0.1 | $3.20 \pm 0.54$ |
| 2001 | Angulo *et al.*[a] [9] | $0.08^{+0.13}_{-0.06}$ | $1.63 \pm 0.17$ | $0.06^{+0.01}_{-0.02}$ | $--$ | $1.77 \pm 0.20$ |
| 2003 | Mukhamedzhanov *et al.* [15] | $0.15 \pm 0.07$ | $1.40 \pm 0.20$ | $0.133 \pm 0.02$ | 0.02 | $1.70 \pm 0.22$ |
| 2004 | Formicola *et al.* [16] | $0.25 \pm 0.06$ | $1.35 \pm 0.05$ (stat) $\pm 0.08$ (sys) | $0.06^{+0.01b}_{-0.02}$ | 0.04 | $1.7 \pm 0.1$ (stat) $\pm 0.02$ (sys) |
| 2005 | Imbriani *et al.* [10] | $0.25 \pm 0.06$ | $1.21 \pm 0.05$ | $0.08 \pm 0.03$ | 0.07 | $1.61 \pm 0.08$ |
| 2005 | Runkle *et al.* [14] | $0.49 \pm 0.08$ | $1.15 \pm 0.05$ | $0.04 \pm 0.01$ | $--$ | $1.68 \pm 0.09$ |
| 2005 | Angulo *et al.* [17] | $0.25 \pm 0.08$ | $1.35 \pm 0.04$ | $0.06 \pm 0.02$ | 0.04 | $1.70 \pm 0.07$ (stat) $\pm 0.10$ (sys) |
| 2006 | Bemmerer *et al.* [12] | $--$ | $--$ | $--$ | $--$ | $1.74 \pm 0.14$ (stat) $\pm 0.14$ (sys)[c] |
| 2008 | Marta *et al.* [13] | $0.20 \pm 0.05$ | $--$ | $0.09 \pm 0.07$ | $--$ | $1.57 \pm 0.13$ |
| 2010 | Azuma *et al.* [18] | 0.28 | 1.3 | 0.12 | 0.11 | 1.81 |
| 2011 | Adelberger *et al.* [2] | $0.27 \pm 0.05$ | $1.18 \pm 0.05$ | $0.13 \pm 0.06$ | 0.08 | $1.66 \pm 0.08$ |
| 2016 | Li *et al.* [19] | $0.42 \pm 0.04$ (stat) $^{+0.09}_{-0.19}$(sys) | $1.29 \pm 0.06$ (stat) $\pm 0.06$ (sys) | $--$ | $--$ | $--$ |
| 2018 | Wagner *et al.* [20] | $0.19 \pm 0.01$ (stat) $\pm 0.05$ (sys) | $1.24 \pm 0.02$ (stat) $\pm 0.11$ (sys) | $--$ | $--$ | $--$ |
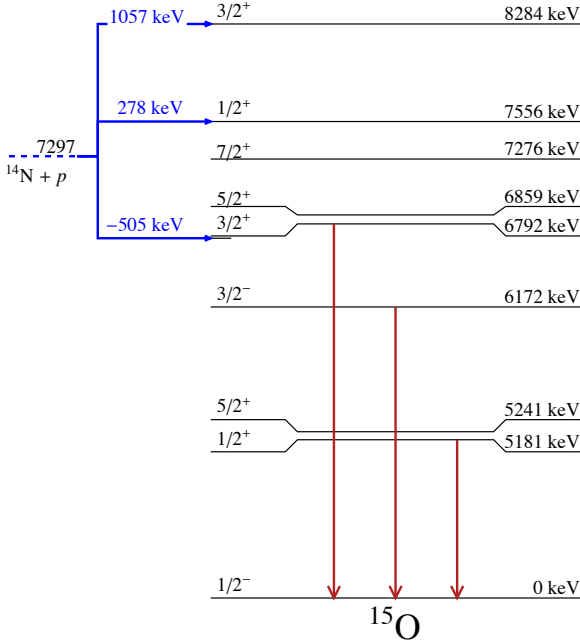


FIG. 1: Level scheme of the $^{15}$O compound nucleus. The resonance (laboratory frame) energies and corresponding excitation energies of the important states are given. As noted, the transitions to the 6792 keV state and ground state are the two strongest and those reported in this work. All of the states at or below the 6792 keV excitation decay with 100% branching to the ground state.

The authors indicated that there was still considerable uncertainty, coming from the background contributions at resonances above 2 MeV, the low-energy ground state transition data, and the width of the subthreshold state at 6.79 MeV.

The most recent measurements were made by Li et al. [19] and Wagner et al. [20]. The experiment in [19] sought to determine the impact of the tails from broad high-energy resonances down at low, astrophysical energies. They took radiative capture data for capture to the 6.79 MeV level in the proton energy range between 1.5 - 3.4 MeV and the range of 0.6 - 3.4 MeV for the DC/R→gs transition. The authors also reported new angular distributions for the reaction. For their extrapolated $S$ factors, the authors reported $S_{6.79}(0) = 1.29 \pm 0.04(stat) \pm 0.09(syst)$ keV b and $S_{g.s.}(0) = 0.42 \pm 0.04(stat)^{+0.09}_{-0.19}(syst)$ keV b. The authors identified the primary, remaining sources of uncertainty as the $\Gamma$ width of the 6.79 MeV state in $^{15}$O, the DC/R→gs transition, and the DC/R→6.17 MeV level primary transition. Critically, the data reported do not overlap with the low energy measurements of the LUNA and TUNL groups and their absolute scale does not align, leading to further inconsistent extrapolations of the reaction behavior at low energies.

Wagner et al. [20] followed up on these results by attempting to bridge the gap between the higher energy data sets of [8, 19] and the low energy data. They focused on the cross section for the transition to the 6.79 MeV state and ground state capture at proton energies between 0.36 and 1.29 MeV. Their reported values for the $S$ factors are $S(0)_{g.s.} = 0.19 \pm 0.05$ keV b and

$S(0)_{6.79} = 1.24 \pm 0.11$ keV b. Looking at their data for the capture to the 6.79 MeV state, particularly above $E_p = 0.8$ MeV, they found cross-sections significantly elevated compared to those of either Schröder et al. [8] or Li et al. [19]. The authors note that following their analysis the capture to the ground state, along with the other weaker transitions, are still a source of significant uncertainty in the reaction data.

New measurements have been published about the $\Gamma$ width of the 6.79 MeV sub-threshold state in $^{15}$O **cite-Frentz2021**. Following the analysis of Li et al. [19], this component was previously the largest source of uncertainty in the low-energy extrapolations of the cross section. The work by **citetFrentz2021** found a lifetime of $\tau = 0.6 \pm 0.4$ fs, placing the most stringent limit on the lifetime, and, therefore, the width of the state. These results, however, when combined with an R-matrix analysis demonstrated that the uncertainty in the lifetime remains too large for significantly reducing the extrapolation for the low energy $S$ factor.

The BOREXINO collaboration has succeeded in the first measurement of the CNO neutrinos associated primarily with the $\beta$ decay of $^{15}$O [21]. Their results suggest an enhanced reaction rate, and therefore cross section, at low energies, more in line with the TUNL data of Runkle et al. [14] versus the data from the LUNA group [10–13]. The low energy extrapolation of the Li et al. [19] data using a comprehensive R=matrix analysis of the radiative capture $^{14}$N(p,$\gamma$)$^{15}$O data over all $\gamma$ channels covering a wide energy range and a broad angle range to take into account the full angular distribution. The R-matrix data based on these fits were not in compliance with the low energy data presented by the LUNA collaboration [10–13] but seem to confirm the data by Runkle et al. [14]. In light of these discrepancies, also in the higher energy data presented by Wagner et al. [20], a new measurement of the $^{14}$N($p, \gamma$)$^{15}$O reaction cross section seems justified covering the energy range between the different data sets in a consistent approach towards a coherent R-matrix analysis including the entire data assembly.

In this work, we detail such a measurement, providing a new and independent cross sections measurements for the two most important transitions in the $^{14}$N($p, \gamma$)$^{15}$O reaction at proton energies between 0.27 and 1.07 MeV. This energy range was chosen to overlap the low energy data from LUNA and TUNL citeImbriani2005, Lemut2006, Bemmerer2006, Marta2008, Runkle2005 with the high energy measurements of [8, 19], like that of Wagner et al. [20]. The experimental details are first discussed in Sec. II, covering the setup and measurement. In Sec. III, the data analysis is explained and the cross sections are presented. $R$-matrix calculations incorporating the new data from this measurement and the recent lifetime results from citeFrentz2020 are described in Sec. IV. Finally, the summary and conclusions are presented in Sec. V.
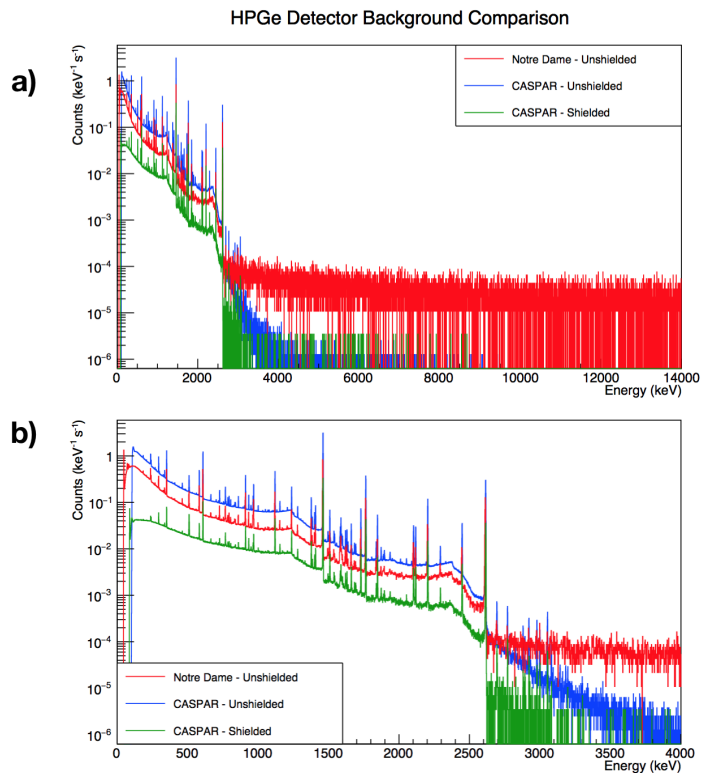


FIG. 2: Background $\gamma$ spectrum taken at CASPAR (with and without lead shielding) and the Notre Dame Nuclear Science laboratory. a) The full spectrum. b) The low-energy subset of the spectrum to highlight the radiogenic background, which is higher at the CASPAR facility when lead shielding is not employed.

## II. EXPERIMENTAL METHODOLOGY

### A. Accelerators and setup

The measurements occurred in three, two-week campaigns over 2018 and were performed using the 1 MV JN Van de Graaff accelerator located at the Compact Accelerator System for Performing Astrophysical Research (CASPAR) at the Sanford Underground Research Facility cite. The primary advantage of the CASPAR facility is the low-background environment created by the rock cover from the Black Hills. Located nearly a mile underground, the rock between the CASPAR facility and the Earth's surface acts as a shield from cosmic rays and decreases the high energy background from cosmic rays in the detector, above 2.6 MeV. This dramatic background reduction is shown in Fig. 2.

The JN was used to produce protons in the range from $E_p = 0.27$ to 1.07 MeV. Typical proton-beam intensities were between 50 and 100 $\mu$A. The energy calibration of this machine was established to better than 1 keV using the well-known $^{27}$Al($p, \gamma$)$^{28}$Si resonance at 992 keV [22] and the $^{14}$N($p, \gamma$)$^{15}$O resonance at 278 keV [23].

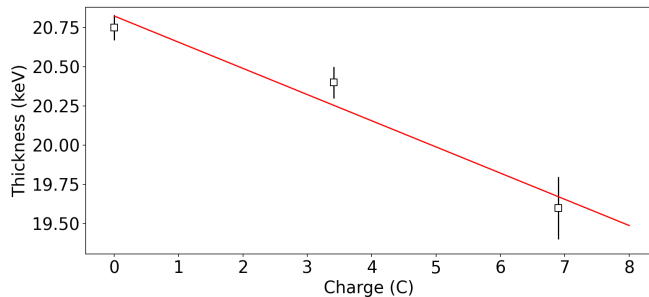Targets were mounted on a 45° target holder, relative

FIG. 3: Typical deterioration of the ZrN targets used in this experiment. The thickness was measured by scanning the $E_p = 278$ keV resonance. This degradation was used to correct for the amount of nitrogen in the target for reach run.
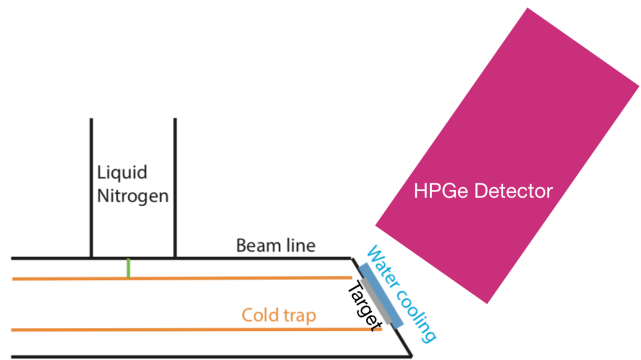


FIG. 4: Schematic of the experimental setup. For clarity, the lead shielding that surrounded the detector during the measurement is not shown.

to the beam axis, and due to the high beam currents, the backings were constantly cooled with recirculating de-ionized water. A copper cold finger, biased to $-400$ V and cooled with a liquid nitrogen reservoir, was utilized to limit carbon build-up and suppress secondary electrons throughout the measurements. The position of the beam on the target was defined by pairs of vertical and horizontal slits to prevent drifting on the face of the targets throughout the course of the runs, some of which lasted several hours.

## B. Targets

The ZrN targets were fabricated by reactive sputtering of Zr in a nitrogen atmosphere in two batches to nominal thicknesses of 50 and 100 nm, respectively. The thicknesses of all targets used in this experiment were measured using the narrow resonance at $E_p = 278$ keV and were found to be $11.2 \pm 0.2$ keV, $11.5 \pm 0.1$ keV, and $20.8 \pm 0.1$ keV, respectively. The stability of these targets were also continuously monitored during the course of the experiment by remeasuring this resonance and monitoring the target profile. Target degradation was observed, shown in Fig. 3. This deterioration was accounted for in the following analysis by correcting for the number of nitrogen atoms in the target for each run.

## C. $\gamma$-ray detector

The de-exciting $\gamma$ rays were observed with a coaxial p-type high-purity germanium (HPGe) detector, of 130% relative efficiency from the University of Notre Dame Nuclear Science Laboratory. A lead sheet of 1.5 mm thickness was placed in front of the crystal's face to attenuate the low-energy $X$ rays entering the detector, reducing the count rate from the low energy background. Lead bricks were placed around the detector to create a shield of at least 10 cm thick on all sides to reduce the radiogenic background from the uranium and thorium decay

chains in the walls of the experimental chamber. The detector was placed at $55°$ relative to the beam axis to minimize angular distribution effects, shown schematically in Fig. 4. Additionally, the detector was on an adjustable table, allowing the detector and lead shielding to be moved closer or further from the target. This was necessary to reduce the high count rate during some of the runs. At the closest, the detector face was 1.0 cm away from the target and 25.4 cm away from the target at the furthest geometry.

## III. ANALYSIS AND RESULTS

### A. Efficiency and summing

The full-energy peak detector efficiency was measured by using transitions from the well-known $E_p = 278$ keV resonance in the $^{14}\text{N}(p, \gamma)^{15}\text{O}$ reaction were used. A polynomial function of 3rd order was used to fit the full-energy-peak (FEP) efficiency [24]

$$\epsilon(E_\gamma) = \exp\left(\sum_{i=0}^{n} a_i \ln(E_\gamma)^i\right). \tag{1}$$

As noted in Sec. II A, the entire detector setup could be moved to different distances from the target and the data were taken in both near and far geometries. At near distances, the count rate is high and summing effects are significant, whereas the count rate is low and there is negligible summing at far distance. Broadly speaking, summing effects arise when multiple photons deposit a portion or all of their energy in the detector at the same time. When this occurs, the individual $\gamma$ peaks are lowered (summing-out) and an artificial count is added at their energy sum (summing-in). With large detection efficiencies or small distances between the detector and source (which we have) the effect of the coincidence summing is significant and must be taken into account. For

sources like $^{137}$Cs, the nucleus decays by emitting one single $\gamma$-ray, meaning no summing effects affect the data. However, the $^{14}$N$(p,\gamma)^{15}$O reaction proceeds through a series of two-step cascades, where every secondary transition has a 100% branching ratio to the ground state, and therefore the summing-out effects on our data must be corrected.

For a primary/secondary pair of decays in a cascade, the summing-out effects can be determined with

$$Y_i^{pri} = RB_i\eta^{FEP}(E_\gamma^{pri})\left(1 - \eta^{TOT}(E_\gamma^{sec})\right) \qquad (2)$$

$$Y_i^{sec} = RB_i\eta^{FEP}(E_\gamma^{sec})\left(1 - \eta^{TOT}(E_\gamma^{pri})\right) \qquad (3)$$

where $i$ denotes a specific transition sequence, $Y_i$ represent the measured yields of the primary and secondary $(pri/sec)$ transitions, $R$ is the number of reactions per incoming particle, $B_i$ are the branching ratios for the respective transitions, and $\eta^{FEP}$ and $\eta^{TOT}$ are the full-energy peak and total efficiencies, respectively [24 **?** ]. Similarly, the contribution of this cascade's pair to a full sum peak, which matches the energy of the ground state transition for the $^{14}$N$(p,\gamma)^{15}$O reaction, can be written as

$$N_{\text{sum}}(E_\gamma^{pri} + E_\gamma^{sec}) = RB_i\eta^{FEP}(E_\gamma^{pri})\eta^{FEP}(E_\gamma^{sec}), \quad (4)$$

because this contribution is the case when the full energy of both transitions are deposited at the same time and the resultant sum-peak's energy matches the ground state transition.

The experimental data from the $E_p = 278$ keV resonance in the $^{14}$N$(p,\gamma)^{15}$O reaction were use to determine the efficiencies. The measurements were taken in different distances between the detector and target, moving the detector stand on rails to ensure the detector remained on the same 55° axis relative to the beam. These different distance measurements allowed us to characterize and correct for the summing effects. The experimental data and corresponding efficiency curves are shown in Fig. 5. All measured yields in close measurement geometry were corrected for summing effects, as can also be seen in the near data of Fig. 5.

### B. Spectrum analysis and fitting procedures

A typical spectrum taken with the HPGe detector of the high-energy region is presented in Fig. 6. These spectra show the population of the $^{15}$O nucleus in the $^{14}$N$(p,\gamma)^{15}$O reaction as the secondary transition from the state at 6792 and the ground state are both prominent. These two $\gamma$-rays, alongside the primary transition of the R/DC $\rightarrow$ 6792 keV excited state, are of most import for this work and are the focus of subsequent analysis.

Well-known contamination lines can also be seen in these spectrum from fluorine in the target backings via
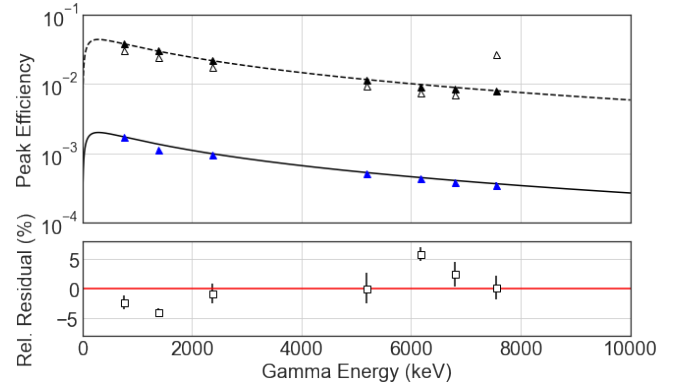


FIG. 5: Results of the efficiency calibration. Top panel: full-energy peak efficiency for a single $\gamma$-ray as a function of energy and detector setup. The two setups involved the detector placed 1.0 cm away from the target and 25.4 cm away, respectively. The open markers are efficiencies uncorrected for summing effects while the full markers include those corrections. The line through the far distance points was fit to the data while the line for the near distance was scaled by the difference in solid angle subtended by the detector in the two distances. Bottom panel: relative residuals between the corrected data and the efficiency curve at the detector distance of 1.0 cm.

the $^{19}$F$(p,\alpha\gamma)^{16}$O reaction at 6130 keV. This peak, which includes a wide Doppler-broadened component underneath a sharp Gaussian peak, overlaps the secondary transition of the 6172 keV excited state in $^{15}$O. This fact, alongside the relatively weak population of the state to begin with, is that no analysis of this transition is attempted in the present (and many other) work.

In fitting the peaks present in the spectra, the centroid, area, and width are determined directly from the bin contents in the histogram. The net area of the peaks were found after removing a cubic background contribution from the spectrum. The background was fit separately, using regions surrounding the peak of interest to increase the fidelity of the background estimation. In this high-energy region of the spectrum, a cubic background is a reasonable assumption, as the background is small and the peaks of interest are typically well isolated from each other. Often, the cubic term is zero after the fit, causing it to become a linear background.

### C. Cross section determination

The excitation function for the transition to the 6.79 MeV state and ground-state of $^{15}$O for the $^{14}$N$(p,\gamma)^{15}$O reaction have been measured in the proton energy range 0.27 to 1.07 MeV.

The experimentally observed yields $Y(E_p)$ were found by correcting the peak areas for the delivered charge, target degradation, detector efficiency, and summing effects. Subsequently, the differential cross-sections are cal-
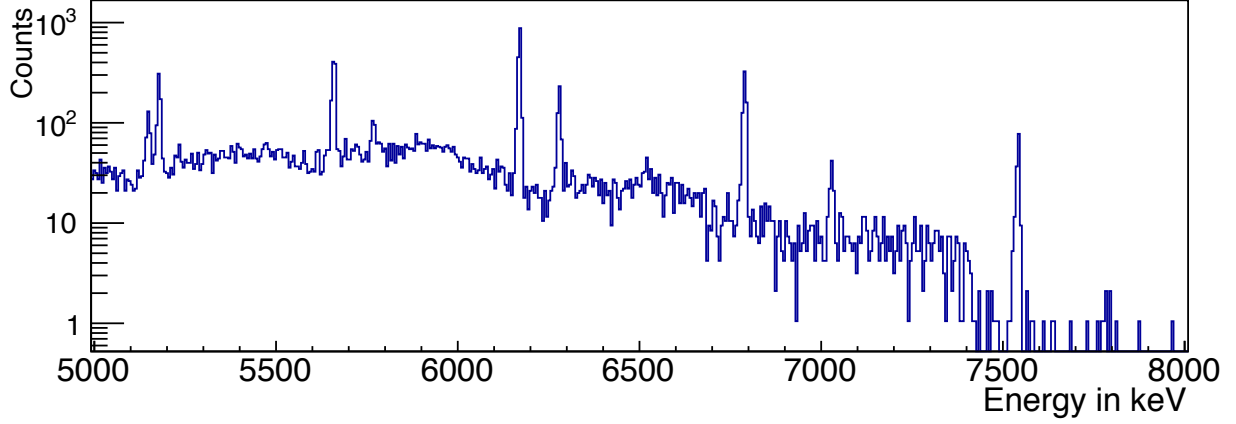
FIG. 6: Typical example of the high-energy part of the $\gamma$-ray spectra obtained in this experiment. Specifically, this is from data taken at $E_p = 270$ keV, with the detector in close geometry, and 1 C of charge delivered to the target during this run.
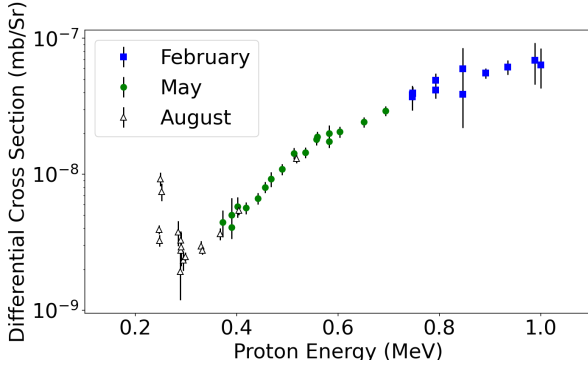


FIG. 7: Differential cross section for the R/DC $\rightarrow$ 6.79 MeV transition, separated by measurement campaign.
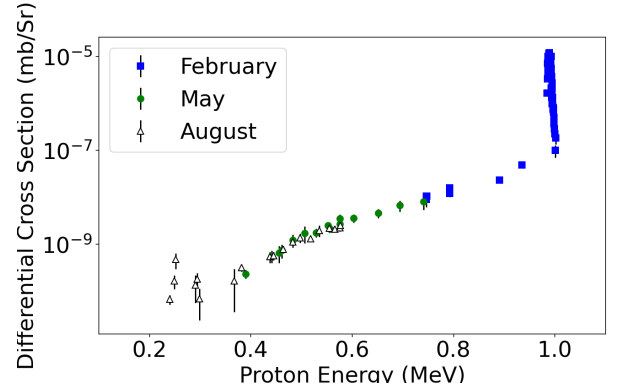


FIG. 8: Differential cross section for the R/DC $\rightarrow$ ground state transition, separated by measurement campaign.

culated from these yields via

$$\sigma(E) = \left(\frac{\lambda_R^2}{2}\right) \frac{\omega\gamma}{\Delta(E_p)} \frac{Y(E)}{Y_{max}(\infty)} \quad (5)$$

where $\lambda_R$ is the de Broglie wavelength of the system, the resonance strength $\omega\gamma = 13.6$ meV was obtained from [2], $Y(E)$ is the yield for a given data point, and $Y_{max}(\infty)$ is the thick target yield on the resonance. The uncertainties are propagated through in quadrature through this calculation.

The resulting differential cross sections and $S$-factors obtained in this work are shown in Figs. 7, 8, 9, and 10. The $S$ factors were calculated using the `AZURE2` code [18] as a part of the fitting (described in Sec. IV. Our data and those of Li et al. [19] were correctly treated as differential for the fitting but were scaled by $4\pi$ for the figure to facilitate comparisons with the literature data.

For the 6.79 MeV transition, our measurement agrees well with the data from Schröder et al. [8] and Li et al. [19] at our high-energy limit but is lower than the data from Wagner et al. [20] in the same energy regime. Our

highest uncertainty data points overlap with the data from Wagner et al. [20] but are otherwise discrepant. Our results agree well with the literature data in the lower-energy region where we overlap with the results from LUNA [10, 13, 16, 25] and Runkle et al. [14]. The full range of the data taken in this work is shown in Fig. 9 alongside the literature measurements.

For the ground state transition, this measurement is in very good agreement with all reported literature data and is shown in Fig. 10. At energies above 800 keV our data lies on the data from Schröder et al. [8] and Li et al. [19]. Our measured $S$ factor drops below the other reported measurements between 800 keV and 600 keV. At energies below this point, our data agrees well with the published data from Runkle et al. [14] and the LUNA data [10, 13, 16, 25], although it has larger uncertainties. In the region between 300-500 keV, right above the resonance, our data continues to agree well with literature. However, our data becomes noticably sparser in this energy regime. WIth such low statistics in the data for these points, most had uncertainties greater than 100% after accounting for all
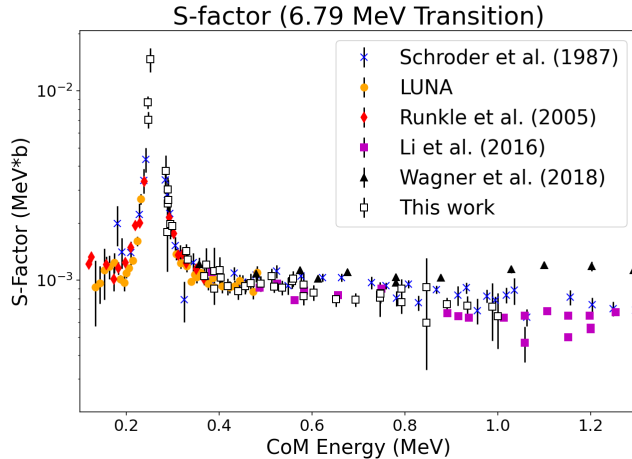
FIG. 9: $S$ factors for the R/DC → 6.79 MeV transition for this work compared with those from Refs. [8, 10–14, 16, 19, 20, 25]. The data series labelled LUNA represents the measurements of [10, 13, 16, 25]. The data from this work and Li et al. [19] have been scaled by a factor of $4\pi$ for the purposes of plotting and comparing to previous works only, the data was treated as differential in calculations. The data from Schröder et al. [8] are corrected [2].
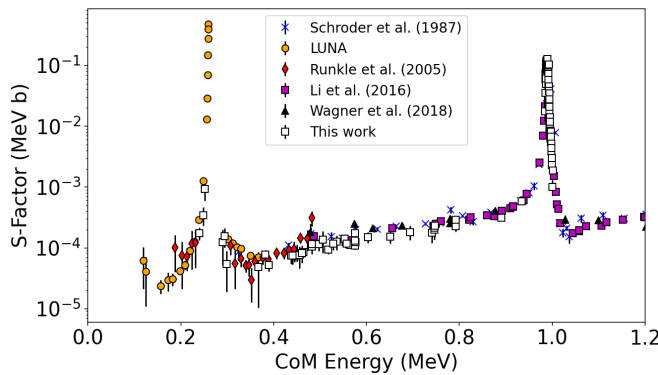


FIG. 10: $S$ factors for the R/DC → ground state transition for this work compared with those from Refs. [8, 10–14, 16, 19, 20, 25]. The data series labelled LUNA represents the measurements of [10, 13, 16, 25]. The data from this work and Li et al. [19] have been scaled by a factor of $4\pi$ for the purposes of comparing to previous works only, the data was treated as differential in calculations. The data from Schröder et al. [8] are corrected [2].

sources of uncertainty and were excluded. The points that we report below the 278 keV resonance are in good agreement with the data taken by the LUNA group.

## IV.  *R*-MATRIX ANALYSIS

An R-matrix analysis [28,29] using the `AZURE2` code [18] was used to simultaneously fit all the ground state and the $E_x = 6792$ keV primary transition differential-cross-section data measured in the current experiment. Only statistical uncertainties were included in the fitting.

The cross-section data utilized in the fitting routine were from measurements at LUNA [10, 13, 16, 25], TUNL [14], Bochum [8], the University of Notre Dame [19], and Dresden [20]. All of these data sets were left without scaling during the fits. The Bochum data from Schröder et al. [8] were corrected as detailed in SFII [2]. The angle-integrated cross sections shown in this work for both the present data and that of Li et al. [19] are calculated by multiplying the differential cross-sections by $4\pi$. It should be emphasized that the angle-integrated cross sections that were determined in this way are only used in plotting for comparison with previous analyses. The R-matrix analysis was performed directly with the differential-cross-section data, in the same way as Li et al. [19].

A channel radius of 5.5 fm was adopted for this work, which matches the analyses done by [2], [19], and [20]. Information about the levels and their parameters as used in `AZURE2` are contained in Table II.

**GIVE MORE CONCRETE DISCUSSION OF THE FINDINGS WHEN FITS ARE FINISHED AND INCLUDE THE FIGURES SHOWING THE FITS.**

## V.  SUMMARY AND CONCLUSIONS

The excitation function of the $^{14}$N$(p,\gamma)^{15}$O reaction has been measured with a HPGe detector from $E_p = 0.27$ to 1.07 MeV for the ground state and 6.79 MeV transitions at the CASPAR facility. These measurements bridge the gap between low-energy measurements of this reaction [10, 13, 14, 16, 25] and those at high energy [8, 19].

A multichannel $R$-matrix analysis was performed simultaneously for both the ground state and $E_x = 6792$ keV transitions. Incorporating recent results for the lifetime of the excited state at 6792 keV, we find that...

Additional measurements of the low-energy ground-state transition could further reduce the uncertainty of the total cross section at stellar energies. This also agrees or disagrees with the findings from Agostini et al. [21] for the solar neutrino flux. This indicates that...

TABLE II: Levels used in the $R$-matrix fits. Bold values indicate parameters which were allowed to vary during the fit. The signs on the partial widths and ANCs indicates the relative interferences. The dividing line demarcates the proton separation energy at $E_x = 7.2968(5)$ MeV [23]. Levels where all parameters are fixed are not shown in this table for brevity but were included in the fits. **OBVIOUSLY MAKE THESE THE REAL PARAMETERS FROM THE FINAL FIT.**

| $E_x$ (Ref. [23]) | $E_x$ (fit) | $J^\pi$ | Channel | l | s | ANC (fm$^{-1/2}$) / Partial Width (eV) |
|---|---|---|---|---|---|---|
| 0.0 | 0.0 | $1/2^-$ | $^{14}$N+p | 1 | 1/2 | 0.23 |
| | | | $^{14}$N+p | 1 | 3/2 | 7.4 |
| 6.7931(17) | 6.7931 | $3/2^+$ | $^{14}$N+p | 0 | 3/2 | 4.75 |
| | | | $^{15}$O+$\gamma_{0.00}$ | E1 | 1/2 | **2.50$^a$** |
| 8.2840(5) | **8.2848** | $3/2^+$ | $^{14}$N+p | 2 | 1/2 | -92.2 |
| | | | $^{14}$N+p | 0 | 3/2 | **4.013×10$^3$** |
| | | | $^{14}$N+p | 2 | 3/2 | -509 |
| | | | $^{15}$O+$\gamma_{0.00}$ | E1 | 1/2 | **0.244** |
| 8.9821(17) | 8.98 | $5/2^-$ | $^{14}$N+p | 1 | 3/2 | **-5.872×10$^3$** |
| | | | $^{15}$O+$\gamma_{0.00}$ | E2 | 1/2 | **-0.303** |
| | | | $^{15}$O+$\gamma_{6.79}$ | E1 | 3/2 | -0.001 |
| 9.484(8) | **9.488** | $3/2^+$ | $^{14}$N+p | 2 | 1/2 | 77.69×10$^3$ |
| | | | $^{14}$N+p | 0 | 3/2 | **126.685×10$^3$** |
| | | | $^{14}$N+p | 2 | 3/2 | -7.822×10$^3$ |
| | | | $^{15}$O+$\gamma_{0.00}$ | E1 | 1/2 | **6.92** |
| 9.488(3) | 9.4905 | $5/2^-$ | $^{14}$N+p | 3 | 1/2 | 0.979×10$^3$ |
| | | | $^{14}$N+p | 1 | 3/2 | -6.576×10$^3$ |
| | | | $^{14}$N+p | 3 | 3/2 | -0.985×10$^3$ |
| | | | $^{15}$O+$\gamma_{0.00}$ | E2 | 1/2 | **-0.307** |
| | | | $^{15}$O+$\gamma_{6.79}$ | E1 | 3/2 | -0.0123 |
| 9.609(2) | 9.6075 | $3/2^-$ | $^{14}$N+p | 1 | 3/2 | **-13.821×10$^3$** |
| | | | $^{15}$O+$\gamma_{0.00}$ | M1 | 1/2 | **1.24** |
| | | | $^{15}$O+$\gamma_{6.79}$ | E1 | 3/2 | -0.044 |
| | 15 | $3/2^+$ | $^{14}$N+p | 0 | 3/2 | **4.722×10$^6$** |
| | | | $^{15}$O+$\gamma_{0.00}$ | E1 | 1/2 | **327.3** |

[1] A. B. McDonald, New Journal of Physics **6**, 121 (2004).
[2] E. Adelberger and a. García, Rev. Mod. ... **83** (2011), arXiv:1004.2318v3, URL http://rmp.aps.org/abstract/RMP/v83/i1/p195{\_}1.
[3] J. N. Bahcall and M. H. Pinsonneault, Phys. Rev. Lett. **92**, 121301 (2004), URL https://link.aps.org/doi/10.1103/PhysRevLett.92.121301.
[4] J. N. Bahcall, A. M. Serenelli, and S. Basu, The Astrophysical Journal Supplement Series **165**, 400 (2006).
[5] M. Asplund, N. Grevesse, and A. Jacques Sauval, Nuclear Physics A **777**, 1 (2006), ISSN 0375-9474, special Isseu on Nuclear Astrophysics, URL http://www.sciencedirect.com/science/article/pii/S0375947405009541.
[6] J. N. Bahcall, S. Basu, M. Pinsonneault, and A. M. Serenelli, The Astrophysical Journal **618**, 1049 (2005).
[7] W. C. Haxton and A. M. Serenelli, The Astrophysical Journal **687**, 678 (2008).
[8] U. Schröder, H. Becker, G. Bogaert, J. Görres, C. Rolfs, H. P. Trautvetter, R. Azuma, C. Campbell, J. King, and J. Vise, Nucl. Phys. A **467**, 240 (1987).
[9] C. Angulo and P. Descouvemont, Nucl. Phys. A **690**, 755 (2001).
[10] G. Imbriani, H. Costantini, A. Formicola, A. Vomiero, C. Angulo, D. Bemmerer, R. Bonetti, C. Broggini, F. Confortola, P. Corvisiero, et al., Eur. Phys. J. A **25**, 455 (2005), ISSN 14346001, 0509005.
[11] A. Lemut, D. Bemmerer, F. Confortola, R. Bonetti, C. Broggini, P. Corvisiero, H. Costantini, J. Cruz, A. Formicola, Z. Fülöp, et al., Phys. Lett. Sect. B Nucl. Elem. Part. High-Energy Phys. **634**, 483 (2006), ISSN 03702693.
[12] D. Bemmerer, F. Confortola, A. Lemut, R. Bonetti, C. Broggini, P. Corvisiero, H. Costantini, J. Cruz, A. Formicola, Z. Fülöp, et al., Nucl. Phys. A **779**, 297 (2006), ISSN 03759474.
[13] M. Marta, A. Formicola, G. Gyürky, D. Bemmerer, C. Broggini, A. Caciolli, P. Corvisiero, H. Costantini,

Z. Elekes, Z. Fülöp, et al., Phys. Rev. C **78**, 1 (2008), ISSN 05562813.

[14] R. C. Runkle, A. E. Champagne, C. Angulo, C. Fox, C. Iliadis, R. Longland, and J. Pollanen, Phys. Rev. Lett. **94**, 082503 (2005), ISSN 0031-9007, URL `http://link.aps.org/doi/10.1103/PhysRevLett.89.262501`.

[15] A. M. Mukhamedzhanov, P. Bém, B. A. Brown, V. Burjan, C. A. Gagliardi, V. Kroha, J. Novák, F. M. Nunes, Š. Piskoř, F. Pirlepesov, et al., Phys. Rev. C **67**, 065804 (2003), ISSN 0556-2813, URL `http://link.aps.org/doi/10.1103/PhysRevC.67.065804`.

[16] A. Formicola, G. Imbriani, H. Costantini, C. Angulo, D. Bemmerer, R. Bonetti, C. Broggini, P. Corvisiero, J. Cruz, P. Descouvemont, et al., Phys. Lett. Sect. B Nucl. Elem. Part. High-Energy Phys. **591**, 61 (2004), ISSN 03702693, URL `http://dx.doi.org/10.1016/j.physletb.2004.03.092`.

[17] C. Angulo, A. E. Champagne, and H. P. Trautvetter, Nucl. Phys. A **758**, 391 (2005).

[18] R. E. Azuma, E. Uberseder, E. C. Simpson, C. R. Brune, H. Costantini, R. J. De Boer, J. Görres, M. Heil, P. J. Leblanc, C. Ugalde, et al., Phys. Rev. C **81**, 1 (2010), ISSN 05562813.

[19] Q. Li, J. Görres, R. J. DeBoer, G. Imbriani, A. Best, A. Kontos, P. J. LeBlanc, E. Uberseder, and M. Wiescher, Phys. Rev. C **93**, 055806 (2016), ISSN 0556-2813, URL `http://link.aps.org/doi/10.1103/PhysRevC.91.045804`.

[20] L. Wagner, S. Akhmadaliev, M. Anders, D. Bemmerer, A. Caciolli, S. Gohl, M. Grieger, A. Junghans, M. Marta, F. Munnik, et al., Phys. Rev. C **97**, 1 (2018), ISSN 24699993.

[21] M. Agostini, K. Altenmüller, S. Appel, V. Atroshchenko, Z. Bagdasarian, D. Basilico, G. Bellini, J. Benziger, R. Biondi, D. Bravo, et al. (2020), 2006.15115.

[22] A. Antilla, J. Keinonen, M. Hautala, and I. Forsblom, Nucl. Instruments Methods **147**, 501 (1977), ISSN 0029554X.

[23] F. Ajzenberg-Selove, Nucl. Physics, Sect. A **523**, 1 (1991), ISSN 03759474.

[24] G. F. Knoll, *Radiation Detection and Measurement* (2000), 3rd ed.

[25] M. Marta, A. Formicola, D. Bemmerer, C. Broggini, A. Caciolli, P. Corvisiero, H. Costantini, Z. Elekes, Z. Fülöp, G. Gervino, et al., Phys. Rev. C **83**, 1 (2011), ISSN 05562813, 1103.5393.